ChevBot – An Untethered Microrobot Powered by Laser for Microfactory Applications

Ruoshi Zhang, *Student Member, IEEE*, Andriy Sherehiy, Zhong Yang, *Student Member, IEEE*, Danming Wei, *Student Member, IEEE*, Cindy K. Harnett, *Member, IEEE*, Dan O. Popa, *Senior Member, IEEE*

***Abstract*—In this paper, we introduce a new class of submillimeter robot (ChevBot) for microfactory applications in dry environments, powered by a 532 nm laser beam. ChevBot is an untethered microrobot propelled by a thermal Micro Electro Mechanical (MEMS) actuator upon exposure to the laser light. Novel models for opto-thermal-mechanical energy conversion are proposed to describe the microrobot's locomotion mechanism. First, an opto-thermal simulation model is presented which is experimentally validated with static displacement measurements with microrobots tethered to the substrate. Then, stick and slip motion of the microrobot was predicted using a dynamic extension of our simulation model, and experiments were conducted to validate this model in one dimension. Promising microrobot designs were fabricated on a silicon on insulator (SOI) wafer with 20µm device layer and a dimple was assembled at the bottom to initiate directional locomotion on a silicon substrate. Validation experiments demonstrate that exposure to laser power below 2W and repetition frequencies below 60 kHz can generate actuator displacements of a few microns, and 46 µm/s locomotion velocity.**

I. Introduction

Autonomous microrobots have been investigated by many in the last few decades, for applications in micro and nano manufacturing, biology, surgery and in-body exploration. In general, microrobots can be classified into those incorporating all necessary power, control and sensor infrastructure onboard [1] [2] [3] [4]and those that harvest the energy and control signals from the environment [5] [6] [7] [8] [9]. Other criteria to classify microrobots depend on the intended applications and environment.

For wet liquid environments, magnetic multi-DOF steering has gained wide acceptance due to biological compatibility and performance [6]. For applications in dry environments, such as in microfactories for nanotechnology, an important subclass of microrobots are those fabricated using MEMS technology on silicon substrate. Regardless the fabrication methods, magnetic, thermal, electrostatic, laser, focused light and piezoelectric effects are all widely used in microrobot actuation for this application. In [4], the authors compared six most popular actuation methods in recent research. The MEMS electrostatic actuator derives its popularity by very low power consumption and reasonable amount of force output, these two merits allow many of those designs to realize untethered operation. Donald et al. [5] demonstrated a MEMS microrobot design driven by electrostatic force on an engineered surface. Thermal actuation is also widely applied on microrobots, often by bimorph or Chevron actuators [4] [10] [11]. Thermal actuators provide high force output while consume highest power among other mechanisms, thus many deisigns are tethered to provide power. There were also significant advancement in the studies of untethered magnetically-powered microrobots [12] [13] [14]. These types of the robots can operate in dry or wet environments, reach relatively high velocities, move on the a variety of surfaces [13] [14], interact with objects [14], and provide excelent motion control. However, systems with magnetically powered robots include external coils of significant size for magnetic field generation, some of the designs require sigificant magnetic fields for operation (1–30 mT) [12] [13] [14], and the devices have to be fabricated from the ferromagnetic material. These factors could be potentially limiting in microfactory applications.

A key limiting factor in advancing microrobot technologies with non-magnetic drives is the delivery of power. Many microrobots have been experimentally demonstrated using tethered power [1], because the reported energy harvesters of that size can only provide power below µW range. In the case of thermal actuators utilizing bimorph or Chevron structures [4] [10] [15] [16], these provide high force output but have to be tethered due to their power requirements. Direct wireless power delivery to miniature robots has several inherent advantages over energy harvested and stored on-board. Under this paradigm, the power required for the operation of the device is externally provided by a dedicated source. The source can also control and communicate with the robot, and this greatly simplifies its internal structure of the microrobot.

The use of light or laser power in microrobotics is motivated by the availability of lasers with high energy concentrations and high directionality. However, its uses have been focused on relatively large dimensional scales (a few mm) and very small scales (below 10 nm). At the millimeter dimensional scale, recent examples of optical actuation include the Robofly [17] in which concentrated laser light beam provides power to a photovoltaic cell then powers actuators and on-board electronics. Optical trapping, is another example of actuation using light energy, but in this case very small forces, pN level, are generated to actuate objects smaller than 10 microns in acqueous media. And thermally driven impingement has also been exploited at the sub-millimeter scale in dry environments for sub-millimetric flight [7] and in liquid media to manipulate biological cells using optically actuated bubbles [8].

The microrobot proposed in this paper, ChevBot, is a new class of MEMS microrobot operating in dry environments,

The authors are with the Electrical and Computer Engineering Department, University of Louisville, Louisville, KY 40292, USA

along planar trajectories, powered and controlled remotely by laser. ChevBot is fabricated from silicon using standard MEMS techniques and offers a unique paradigm for actuation at sub-millimeter scale, combining stick-and-slip locomotion gaits with optically induced thermal actuation without the need to use additional means, such as engineered surfaces or electrostatic clamping. The main target application for ChevBot is to provide the mobile robot equivalents, e.g. part transport in future microfactory applications.

ChevBot was fabricated on an SOI wafer with 20µm device layer, with lateral dimensions of 520µm. Additional dimple was assembled on the microrobot "belly" to reduce thermal dissipation and friction/stiction with the substrate below. The performance of ChevBot was predicted by our previous model developed in [10], however, at that time the laser energy and power levels needed to realize locomotion were unknown. Although actuation may also occur at other laser wavelengths, in this paper we investigate locomotion of the ChevBot when exposed to a 532 nm PWM Nd:YAG laser unit with variable power and repetition frequencies. We refined and experimentally validated a static opto-thermal conversion model as well as a dynamic opto-thermo-mechanical model. Two sets of experiments were conducted to validate simulations: first, steady state experiments measured the displacement generated by the thermal actuator under laser energy at varying levels of power and repetition rates; second, the displacement measurements were used to validate a lumped model of the microrobot; third, experiments were conducted to observe the microrobot locomotion and measure its velocity, and fourth, the results were used to validate the dynamic stick-and-slip simulation model. The purpose of the simulation model is to study and predict the effect of design variables to the expected motion of the microrobot prior to further fabrication. Validation experiments demonstrate that the laser actuation technique is well suited for microrobot locomotion in dry environments and can generate in excess of 40 µm/s locomotion velocity.

This paper is organized as follows: section II describes the physical design and the geometry of the ChevBot; section III provides details about fabrication, assembly, and the laser experimental setup; section IV presents results of the steady state simulation and actuator displacement measurements; Section V focusses on dynamic (stick-and-slip) model and ChevBot's locomotion experiment; finally, section VI concludes the paper and discusses future work.

II. Physical Dimensions of ChevBot and Mode of Operation

The physical design of the ChevBot undertaken in this paper is based on simulation models detailed in [10], which predicted velocity of a few mm per second in response to the laser pulsed signal in the kHz range. In this work, variations of the design have been fabricated and used to experimentally validating a static and dynamic model.

The ChevBot depicted in Figure 1 is composed of a body frame, to which 12 thin beams acting as a Chevron actuator are fixed on both sides and meet at the center shuttle. Two "feet" are connected to the external side of the shuttle and they are in contact with the operation surface after assembly. The dimple is a piece of square-shaped silicon 80µm wide and 20 µm thick, fabricated on the same wafer, and assembled to the center of the body frame. The evenly distributed holes in the body frame help reduce release process time. The ChevBot is 260µm × 520µm in size, and 40µm tall after the dimple is assembled. The beam features the thinnest part of 5µm wide, 200µm long and forms 87.14° angle with the body frame. In Figure 1, the green ellipse indicates the shape and location of the laser spot on the robot's body during actuation.

Figure 1 A bottom-up and side views illustration of the ChevBot. The green oval represents the laser spot on the microrobot's body.

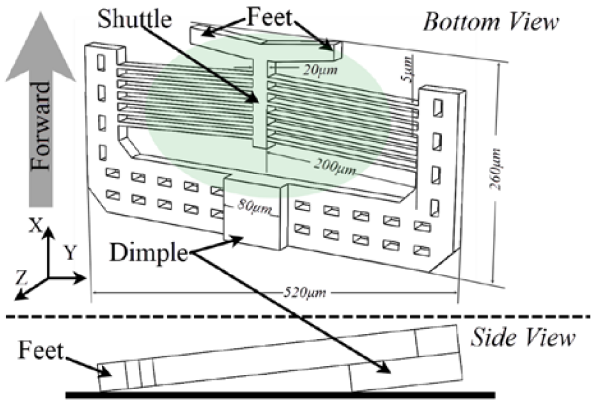

The ChevBot and the substrate form a three-point contact configuration including two contacts at the feet and one along the edge of the dimple. Figure 2 depicts a mass-spring diagram illustrating the ChevBot's stick-and-slip gaiting motion. This model simplifies the feet and dimple into two blocks with masses m_1 and m_2, respectively and simplifies the thermal actuator into a weightless spring. During a laser on period, the dimple sticks to the surface and the feet slip forward; when the laser is switched off, the feet stick and the dimple slips forward to achieve a gaiting cycle.

Figure 2. Illustration of ChevBot's stick-and-slip locomotion.

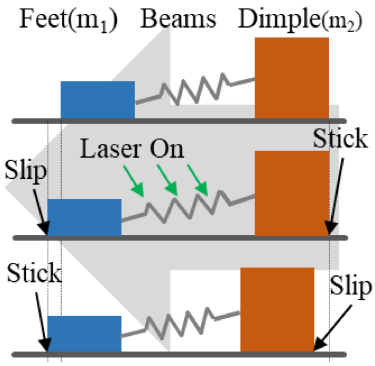

III. Fabrication, Assembly and Laser Test Bench

In this section, we describe the fabrication process of the microrobot, and the experimental set up for the laser actuation measurements. The whole fabrication process of the ChevBot has three major steps: photolithography mask design, the silicon body fabrication, and the dimple assembly.

A. Clean Room Fabrication Process

The ChevBot was fabricated on a 4-inch SOI wafer with 20µm device layer, <100> orientation and 2µm of buried oxide layer. The wafer was firstly cleaned to remove any

contamination on the surface, then a layer of 3µm thick photoresist (SPR220-3.0) was applied, exposed and developed, which defines the shape of ChevBot and serves as a subsequent masking layer for the deep reactive ion etching (DRIE) process. The baking temperature in this process needs to follow a ramp up and down profile to avoid cracks on the photoresist surface. Then, a DRIE process was performed to carve out the microrobot's body and then diced into individual dies. Finally, each die was released by soaking into 49% hydro-fluoric acid for 20 minutes. The samples were dried right after releasing process using a critical point drier (CPD).

B. Assembly with the NeXus Microassembly Station

The NeXus micro-assembly station is a customized multi-stage micro manipulation system, shown in Figure 3. It consists of three cameras providing a top-down, a horizontal and an angled view (EO-3112C, EO-6412C and EO-1312C) of the assembly site and two manipulators M1 and M3. M1 provides three degree-of-freedom (DOF) of motorized X, Y and rotational (θ), from bottom to top. The sample chuck is fixed on top of the θ stage. M3 is half-motorized with 7 DOFs: a manual Z at the bottom, motorized X, Y, Z and θ, and tip, tilt on the end-effector adapter. The end-effector is a vacuum dispenser (SMD-VAC-HP) with 90° tip fixed onto the θ stage with a 3D printed adapter.

Figure 3. NeXus assembly station.

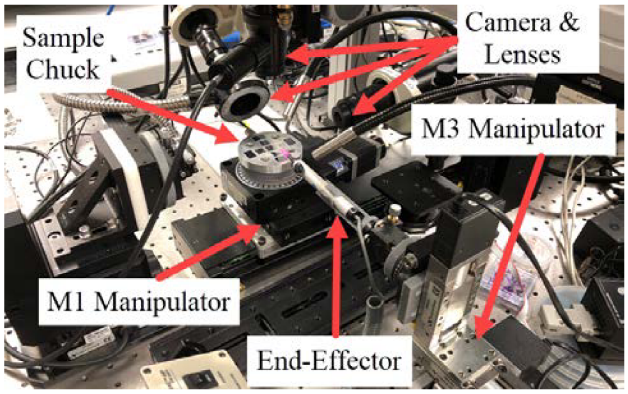

The dimple was attached onto the body frame via UV adhesive (BONDIC® L4G 3V5, Aurora, ON, Canada), for it has appropriate viscosity and withstands the temperature during laser actuation experiment. To assemble the dimple onto the ChevBot, the dimple was firstly dipped into the adhesive and then translated and aligned with the assembly location; then the M3 stage lower its end-effector to finish the attachment process. After contact, an UV flash light is used to solidify the adhesive.

C. The Laser Test Bench

A test bench was developed to conduct laser irradiation tests for both steady state and locomotion test. Considering that steady state tests involve measurements only of the actuator's displacement, the microrobot was tethered to the substrate. However, for locomotion tests, a X-Y positioning stage holding the sample was used to compensate the microrobot motion so that the laser spot was always delivered on the center of the actuator. The components of the testing bench consist: An Explorer One HE 532-200 from Spectra-Physics; laser displacement sensor LK-H008 from Keyence; system of lenses, long distance microscope objective, neutral density filters and mirrors; X-Y positioning stage from Newport (443 and 433 Series) and, sample chuck; tube lens, illuminator and a Pixelink CMOS camera. Shown in Figure 4.

Figure 4 presents schematic view of the testing bench. The laser beam is passed through the neutral density filters and system of the lenses, toward the set of the adjustable mirrors, that direct laser beam onto the ChevBot. The laser beam is at 45° angle to the normal of the sample's surface. Thus, the laser spot has an elliptical shape on the actuator. A camera with microscope objective lens is placed above the sample chuck for the visual feedback. The resulting optimal size of the laser beam was large waist diameter of wd_{max} = 300µm and small waist dimeter of wd_{min} = 240µm.

Figure 4. The schematic of the laser testing bench.

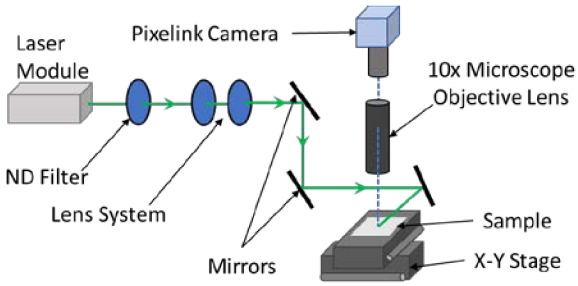

IV. Steady State Modeling and Experiments

This section presents results of the simulation and series of experiments required to evaluate the response of ChevBot to different levels of laser power and repetition rate. The results of this characterization are later used in developing dynamic model.

A. Simulation Model for Steady State Analysis

A steady-state model was constructed and implemented using MATLAB Simulink® to simulate the opto-thermal-mechanical behavior of ChevBot. The model has three components: an optical heating model, a thermal dissipation model describing heat distribution process in the robot's body with boundary conditions, and a mechanical expansion model based on the resulting thermal loading [10]. The constants used in the simulation is shown in Table I. This model considered the case of the microrobots tethered to the substrate for comparison with actuator's displacement measurements.

Table I. Values of the Constant Used in the Simulation for the Steady State Analysis

Constant	Quantity/Name	Value
R	Reflectivity of Silicon	0.3
T_{env}	Environment Temperature	20 ℃
ρ_{Si}	Silicon Density	$2328\ \mathrm{kg \cdot m^{-3}}$
h_{air}	Air convection constant	$10\ \mathrm{W \cdot (m^2 \cdot K)^{-1}}$
k_{air}	Air thermal conductivity	$0.025\ \mathrm{W \cdot (m \cdot K)^{-1}}$
c_{v-air}	Air specific heat	$716\ \mathrm{J \cdot (Kg \cdot K)^{-1}}$
k_{Si}	Silicon thermal conductivity	$124\ \mathrm{W \cdot (m \cdot K)^{-1}}$
$c_{v,Si}$	Silicon specific heat	$702\ \mathrm{J \cdot (kg \cdot K)^{-1}}$
α_{Si}	Silicon coefficient of thermal expansion	$2.6 \times 10^{-6}\ (℃)^{-1}$
θ	Theta (beam angle)	0.05 rad

Figure 5. Block diagram of simulation model.

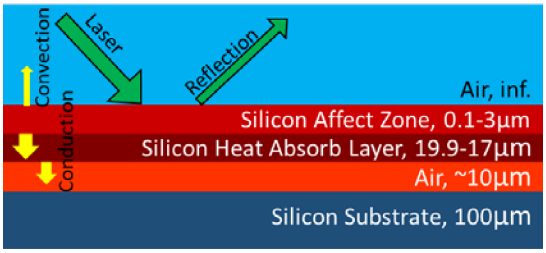

When laser is directed onto the thermal actuator, a portion of radiation energy is converted to heat actuator, while the rest is reflected and lost (Figure 5). The heat energy Q generated at the silicon surface can be described as [18] [19] [20]:

$$dQ = (1 - R)E_e \cdot A, \quad (1)$$

where the R is the surface reflectivity, E_e is the irradiation in J/m^2 and A is the laser spot area in m^2.

In Simulink®, this effect was simulated with the help of lumped first order model which assumes that the illuminated volume of the microrobot can be lumped into a hexahedron shaped silicon structure with the same thickness and surface area, thus the hexahedron becomes the equivalent of the laser heated part of the thermal actuator. The laser induces a temperature change in the silicon according to:

$$\frac{dT}{dt} = \frac{dQ}{c \cdot m}, \; m = \rho V, \; V = \tau A, \quad (2)$$

where τ is the thickness of the material, c is the specific heat capacity and ρ is the material's density. A portion of converted heat is lost due to thermal conduction, convection and radiation. The air gap between the microrobot actuator and the substrate is less than 10μm, which causes heat loss by thermal conduction. The prevalence of conduction over convection has long been established in electrothermal MEMS actuation with a thin gap from the substrate [10] [18] [19]. The top surface of the microrobot has direct contact with air, resulting in heat losses due to convection; and losses due to radiation are assumed to be negligible. The thermal conduction and air convection are governed by:

$$\text{thermal conduction: } \frac{dT}{dt} = -\frac{k}{\rho \tau^2 c}(T - T_\infty), \quad (3)$$

$$\text{air convection: } \frac{dT}{dt} = -\frac{h}{\rho \tau c}(T - T_\infty), \quad (4)$$

where the k is thermal conductivity, T_∞ is environment temperature, and h is the convection constant. After determination of the heat transfer extracted from above model, the displacement caused by thermal expansion can be evaluated. The total deformation of the shuttle can be expressed by [11]:

$$\Delta L = \alpha \Delta T L, \quad (5)$$

$$\Delta d_T = [L^2 + 2L(\Delta L) - L\cos^2(\theta)]^{\frac{1}{2}} - L\sin(\theta), \quad (6)$$

where ΔL is the length change on the beam due to temperature change, L is original length of the beam of the actuator, α is the thermal expansion coefficient, and θ is the acute angle of the beam formed with the shuttle on the thermal actuator. Finally, the expected force output of the actuator is given by [15] [21]:

$$F_a = \frac{2NAE\sin^2(\theta)}{L}\Delta d_T, \quad (7)$$

where the N is number of beams of the actuator – 6 pairs in our case. A is cross-section area, E is Young's modulus.

B. Displacement Measurement Experiments

A series of experiments were conducted to determine the steady-state displacement of the thermal actuator upon laser irradiation. As mentioned in section III, the laser spot has an elliptic shape (Figure 1). Therefore, to maximize the heating efficiency, the major axis of the ellipse is aligned with the longitude of the ChevBot's thermal actuator. Before recording displacement measurements, experiments were conducted to determine the damage threshold for average power, repetition rate and laser spot size. The actuation displacement, Δd, was determined for two laser parameters: average power (Pave) and repetition rate (f). The average power was varied from 0.2W to 1.1W for six different repetition rates in the range 10-60 kHz. The microrobot structure was exposed to the laser light for 2 seconds in order to reach an equilibrium when the thermal actuators stop extending. Results are shown in Figure 6. Maximum displacement of the actuator, approximately 1.4μm, is reached for laser light average power 1.1 W and f = 50 kHz.

Figure 6. Dependence of shuttle displacement (Δd) on the laser average power (P), for given repetition frequency (f).

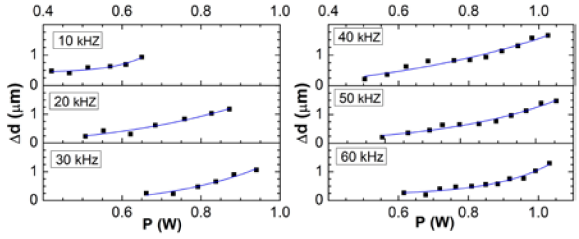

C. Steady State Simulation Model Validation

To validate the opto-thermal simulation model, average power Pave and repetition rate f were fed into Simulink® to estimate actuator deformation.

Figure 7. Maximum displacement (Δd_{max}) vs. maximum average laser power for repetition frequencies (10 – 50 kHz) – experimental data and simulation result from our model.

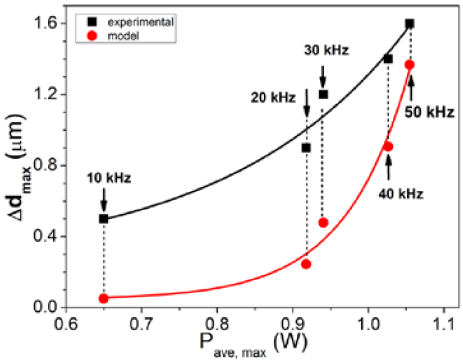

Figure 7 presents actuator's maximum displacement values for the delivered average laser power and repetition rate

f, and shows that both experimental and simulation results follow similar trends. However, displacement values estimated by our model are consistently lower compared to the experiment, possibly due to lumped model approximations, choice of constants, and silicon hexahedron equivalent used in our laser spot model.

V. Dynamic Model and Untethered ChevBot Motion

In this section we propose and validate a simple 1-dimensional dynamical model of the ChevBot's untethered motion in order to estimate the velocity of the microrobot when operating on a flat substrate. This model integrates the steady-state opto-thermal response of section IV with stick-and-slip dynamics.

A. Simulation Model for Dynamic Analysis

The dynamical model of the ChevBot was approximated as a simple rigid body consisting of two sections attached at point C, shown in Figure 8. The AC section represents the Chevron actuator with variable length $L+\Delta d$, and BC is the constant height (h) of dimple. In this diagram, the operating substrate is along the x axis (AB), and the independent variables are x_1, the dimple's x coordinate, and x, the center of mass (CMS) of the ChevBot. The shuttle's leg position x_2 is considered as a dependent variable.

Figure 8. Free body diagram of ChevBot – sideview.

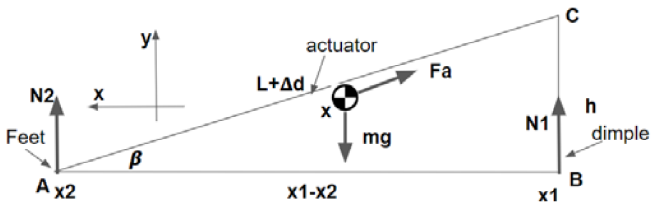

The actuator deformation Δd from (6) generates instantaneous actuator force F_a from (7) and can be used as input to the dynamic model. The tilt angle between microrobot and substrate β is initially approximately 5° and decreases during actuation and extension of the robot's body.

From the force and torque balance equation in the vertical y direction, the surface reaction forces N_1 and N_2 acting on the dimple and the leg can be determined. Assuming that the microrobot moves toward positive x direction, motion of the dimple (x_1) and overall body/CMS (x) can be described by:

$$F_a\cos(\beta) - \mu N_1 - b\dot{x}_1 = \frac{(x_1-x)m}{x_1-x_2}\ddot{x}_1, \qquad (8)$$

$$-F_a\cos(\beta) + (N_1 - N_2)\mu - b\dot{x} = m\ddot{x}, \qquad (9)$$

where $\mu = 0.35$ is the coefficient of friction and b is the viscous damping b = 6.8×10^{-5}kg/s. μN_1 and $(N_1 - N_2)\mu$ represent frictional forces acting on the dimple and center of mass; $F_a\cos(\beta)$ is the x component of the driving force, and $b\dot{x}_1$, $b\dot{x}$ are damping forces. Furthermore, the position of the microrobot's leg x_2 and angle β (both dependent variables) can be determined from:

$$x_1 - x_2 = \sqrt{(L-\Delta d)^2 - h^2},\ \sin(\beta) = \frac{h}{L-\Delta d}, \qquad (10)$$

where $L - \Delta d$ is a function of time – the displacement of the thermal actuator due to laser irradiation.

The stick and slip motion can be simulated by solving (8) and (9) with respective constraint (10) – representing changes to the microrobot length (x_1-x_2) and tilt angle β.

Simulation is based on above equations of the motion with respective constraints were carried out in Simulink®. Figure 9 presents plots of the changes of the position of CMS, as a function of time for different values of the repetition frequency and the power density of the laser. The width of the laser pulse was kept constant (10ns in consistence with experimental parameters of our pulsed laser). Simulation results derived from our dynamic model (Figure 9) suggest that untethered ChevBot would move with a constant speed upon exposure to the laser light.

Figure 9. Changes of the position of center of mass (x) as a function of time for different values of repetition frequency and irradiance.

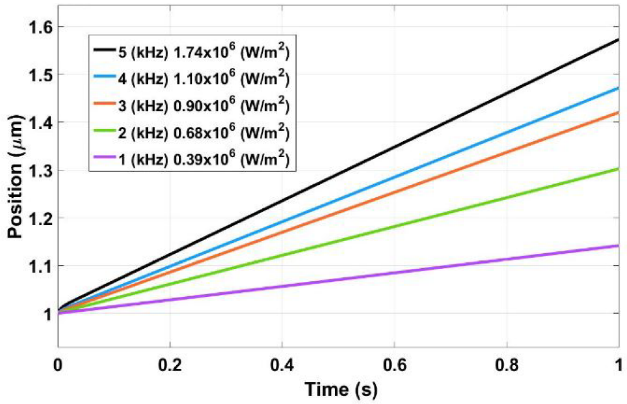

From Figure 9, we notice that increasing the laser power density and repetition rate f would increase the locomotion speed. Thus, indicating that by tuning the parameters of the laser (repetition rate and average power), it is possible to control dynamic properties of the ChevBot.

B. Velocity Measurement Experiments

To validate the stick-and-slip dynamic model, an assembled ChevBot was placed on a piece of silicon substrate, then it was fixed onto the sample chuck of the X-Y stage of the optical setup. The laser spot was fixed around center in the field of view of the camera (Figure 10). In this manner we can control the position of the laser spot relative to the ChevBot by manually adjusting the X-Y stage. At the beginning of the experiment, the microrobot was translated to the area eradiated by the laser, and in a result, it was set into motion.

Figure 10. Two frames extracted from recorded video to calculate the average velocity. Laser repetition frequency: 5kHz. Average power: 60mW.

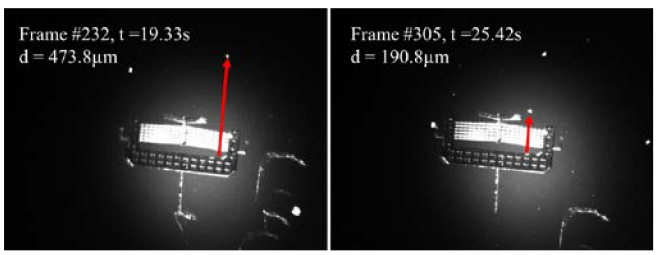

The motion of the microrobot was analyzed based on video frames acquired during the experiment. Since the laser spot location is fixed and only the X-Y stage is compensating

the ChevBot's motion, a piece of dust (a bright dot in Figure 10) on the substrate is chosen as the reference point to determine the traveled distance. The velocity of the microrobot can be estimated by selecting critical frames indicating initial and final position points and corresponding times – as represented by two frames from Figure 10 where displacement is about 283μm and corresponding time interval about 6s.

The calculated velocity of ChevBot was 46.5μm/s which is lower compared to the one determined by simulation under similar conditions (~56μm/s). This discrepancy could be due to the silicon substrate surface quality, dust particles, and the model discrepancies.

VI. Conclusion

An untethered microrobot powered by pulsed laser actuation is presented in this paper. The ChevBot is a MEMS based microrobot locomote with stick-and-slip motion. Wireless actuation of the robot is accomplished by a pulsed laser with powers below 2W, frequencies below 60 kHz, and microrobot velocities of approximately 46.5μm/s. Results of two sets of experiments are presented in this paper designed to validate the steady-state and dynamic locomotion regimes of the microrobot under varying laser power and frequencies. Results show that there is trend-wise agreement between the simulation and experiment.

In future work, we will extend the robot dynamical model to include planar (*x, y*) motions, multiple leg designs, and friction/stiction conditions. We will also work on controllers to coordinate the motion of microrobot and laser spot, and to accomplish controllable trajectories as needed in micro/nanomanipulation tasks.

Acknowledgment

This work was supported by NSF Grant 1734383. We wish to thank the Micro Nano Technology Center staff at the University of Louisville, for their help with fabrication.

References

[1] Y. Chen, H. Wang, E. F. Helbling, N. T. Jafferis, R. Zufferey, A. Ong, K. Ma, N. Gravish, P. Chirarattananon, M. Kovac and R. J. Wood, "A biologically inspired, flapping-wing, hybrid aerial-aquatic microrobot," *Science Robotics,* vol. 2, no. 11, 25 Oct 2017.

[2] A. G. Dharmawan, H. H. Hariri, S. Foong, G. S. Soh and K. L. Wood, "Steerable Miniature Legged Robot Driven by a Single Piezoelectric Steerable Miniature Legged Robot Driven by a Single Piezoelectric," in *2017 IEEE International Conference on Robotics and Automation (ICRA)*, Singapore, May 29 - June 3, 2017.

[3] S. A. Rios, A. J. Fleming and Y. K. Yong, "Design and Characterization of a Miniature Monolithic Piezoelectric Hexapod Robot," in *2016 IEEE International Conference on Advanced Intelligent Mechatronics (AIM)*, Banff, Alberta, Canada, July 12–15, 2016.

[4] E. Y. Erdem, Y.-M. Chen, M. Mohebbi, J. W. Suh, G. T. A. Kovacs, R. B. Darling and K. F. Böhringer, "Thermally Actuated Omnidirectional Walking Microrobot," *Journal of Microelectromechanical Systems,* vol. 19, no. 3, pp. 433-442, June 2010.

[5] B. R. Donald, C. G. Levey, C. D. McGray, I. Paprotny and D. Rus, "An Untethered, Electrostatic, Globally Controllable MEMS Micro-Robot," *Journal of Microelectromechanical Systems,* vol. 15, no. 1, pp. 1 - 15, February 2006.

[6] P. Ryan and E. Diller, "Five-Degree-of-Freedom Magnetic Control of Micro-Robots Using Rotating Permanent Magnets," in *2016 IEEE International Conference on Robotics and Automation (ICRA)*, Stockholm, Sweden, May 16-21, 2016.

[7] S. Ward, V. Foroutan, R. Majumdar, O. Mahdavipour, S. A. Hussain and I. Paprotny, "Towards Microscale Flight: Fabrication, Stability Analysis, and Initial Flight Experiments for 300 μm × 300 μm × 1.5 μm Sized Untethered MEMS Microfliers," *IEEE Transactions on Nanobioscience,* vol. 14, no. 3, pp. 323-331, April, 2015.

[8] W. Hu, K. S. Ishii and A. T. Ohta, "Micro-Assembly Using Optically Controlled Bubble Microrobots In," in *2012 IEEE International Conference on Robotics and Automation*, Saint Paul, MN, USA, May 14-18, 2012.

[9] F. R. Szabo and P. E. Kladitis, "Design, Modeling and Testing of Polysilicon Optothermal Actuators for Power Scavenging Wireless Microrobots," in *2004 International Conference on MEMS, NANO and Smart Systems (ICMENS'04)*, Banff, AB, Canada, Canada, 25-27 Aug. 2004.

[10] M. R. Pac and D. O. Popa, "3-DOF Untethered Microrobot Powered by a Single Laser Beam Based on Differential Thermal Dynamics," in *2011 IEEE International Conference on Robotics and Automation*, Shanghai, China, 9-13 May 2011.

[11] M. Tecpoyotl-Torres, J. Varona, A. A. Hamoui, J. Escobedo-Alatorre and J. Sanchez-Mondragón, "Polysilicon thermal micro-actuators for heat scavenging and power conversion," in *Proceedings Volume 7043, High and Low Concentration for Solar Electric Applications III*, San Diego, California, United States, 2008.

[12] C. Pawashe, S. Floyd and M. Sitti, "Modeling and Experimental Characterization of an Untethered Magnetic Micro-Robot," *The International Journal of Robotics Research,* vol. 28, no. 8, pp. 1077-1094, 2008.

[13] D. R. Frutiger, K. Vollmers, B. E. Kratochvil and B. J. Nelson, "Small, Fast, and Under Control: Wireless Resonant Magnetic Micro-agents," *The International Journal of Robotics Research,* vol. 29, no. 5, pp. 613-636, 2010.

[14] W. Hu, G. Z. Lum, M. Mastrangeli and M. Sitti, "Small-scale soft-bodied robot with multimodal locomotion," *Nature,* vol. 554, pp. 81-85, 2018.

[15] M. R. Pac and D. O. Popa, "Laser-Powered Sub-mm Untethered Microrobots," in *Proceedings of the ASME 2010 Design and Engineering Technical Conferences & Computers and Information in Engineering Conference*, Montreal, Quebec, Canada, August 15-18, 2010.

[16] R. Murthy, A. Das and D. O. Popa, "ARRIpede: A Micro Crawler/Conveyor Robot Constructed via 2 ½ D MEMS Assembly," in *2008 IEEE/RSJ International Conference on Intelligent Robots and Systems*, Nice, France, 22-26 Sept. 2008.

[17] J. James, V. Iyer, Y. Chukewad, S. Gollakota and S. B. Fuller, "Liftoff of a 190 mg Laser-Powered Aerial Vehicle: The Lightest Wireless Robot to Fly," in *2018 IEEE International Conference on Robotics and Automation (ICRA)*, Brisbane, Australia, May 21-25, 2018.

[18] L. Lévesque, "Law of cooling, heat conduction and Stefan-Boltzmann radiation laws fitted to experimental data for bones irradiated by CO2 laser," *Biomedical Optics Express,* vol. 5, no. 3, pp. 701-712, 2014.

[19] F. P. Incropera, Introduction to Heat Transfer 6th Edition, John Wiley & Sons, Inc., 2011.

[20] M. A. Green, "Self-consistent optical parameters of intrinsic silicon at 300 K including temperature coefficients," *Solar Energy Materials and Solar Cells,* vol. 92, no. 11, pp. 1305-1310, 2008.

[21] L. Que, J.-S. Park and Y. B. Gianchandani, "Bent-beam electrothermal actuators-Part I: Single beam and cascaded devices," *Journal of Microelectromechanical Systems,* vol. 10, no. 2, pp. 247 - 254, Jun 2001.